Journal of Wind Engineering & Industrial Aerodynamics 168 (2017) 288–296

Contents lists available at ScienceDirect

Journal of Wind Engineering & Industrial Aerodynamics

journal homepage: www.elsevier.com/locate/jweia

Algorithm for damage detection in wind turbine blades using a hybrid dense sensor network with feature level data fusion

Austin Downey [a,*], Filippo Ubertini [b], Simon Laflamme [a,c]

[a] Department of Civil, Construction, and Environmental Engineering, Iowa State University, Ames, IA, USA
[b] Department of Civil and Environmental Engineering, University of Perugia, Perugia, Italy
[c] Department of Electrical and Computer Engineering, Iowa State University, Ames, IA, USA

ARTICLE INFO

Keywords:
Wind turbine blades
Structural health monitoring
Capacitive-based sensor
Soft elastomeric capacitor
Flexible membrane sensor
Sensor network
Signal decomposition
Damage detection
Damage localization
Data fusion

ABSTRACT

Damage detection in wind turbine blades requires the ability to distinguish local faults over a global area. The implementation of dense sensor networks provides a solution to this local-global monitoring challenge. Here the authors propose a hybrid dense sensor network consisting of capacitive-based thin-film sensors for monitoring the additive strain over large areas and fiber Bragg grating sensors for enforcing boundary conditions. This hybrid dense sensor network is leveraged to derive a data-driven damage detection and localization method for wind turbine blades. In the proposed method, the blade's complex geometry is divided into less geometrically complex sections. Orthogonal strain maps are reconstructed from the sectioned hybrid dense sensor network by assuming different bidirectional shape functions and are solved using the least squares estimator. The error between the estimated strain maps and measured strains is extracted to define damage detection features that are dependent on the selected shape functions. This technique fuses sensor data into a single damage detection feature, providing a simple and robust method for inspecting large numbers of sensors without the need for complex model driven approaches. Numerical simulations demonstrate the proposed method's capability to distinguish healthy sections from possibly damaged sections on simplified 2D geometries.

1. Introduction

Wind energy growth is driven at the nexus of public policy and economics (Borenstein, 2012). As with most renewable energy projects, a wind farm's economic viability typically relies on public subsidies, a predictable energy source, and mature and reliable technology (Afanasyeva et al., 2016). The economic evaluation of wind projects is particularly challenging due to the unpredictable operation and maintenance (O&M) costs. O&M traditionally includes the cost of all necessary repairs and replacements. The estimation of O&M costs for wind generating facilities is difficult as operational lifetime data is insufficient or inapplicable to the quickly evolving energy infrastructure. Therefore, O&M costs are estimated on a cost per MW hours basis, allowing owners to share O&M costs across multiple turbines. However, this practice is less convenient for operators of small wind farms where the ability to hedge cost is difficult (Celik, 2003), for operators of wind farms in micro grids where downtime is often compensated for with expensive fossil fuels (VanderMeer and Mueller-Stoffels, 2014), and for operators of wind farms in the offshore environment where the cost structure is often largely unknown (Cockerill et al., 2001).

Reduction of uncertainty related to the O&M of a wind turbine structural system (Ghoshal et al., 2000) and the enabling of prognostics and health management (PHM) (Richards et al., 2015; Ekelund, 2000) is therefore of interest to wind farm owners and operators. Monitoring the mesostructures (e.g. towers and blades) of wind turbines is difficult due to the need to distinguish between faults in the structure's global (e.g. changing load paths, loss in global stiffness) and local (e.g. crack propagation, composite delamination) conditions (Ghoshal et al., 2000). Traditional approaches for structural health monitoring (SHM) of wind turbine blades have focused on monitoring the structure using a limited number of sensors and applying a variety of post-processing techniques (Gross et al., 1999). However, these techniques often lack the ability to distinguish local failures from global events and demonstrated a limited damage localization ability (Zou et al., 2000).

A logical solution to the local/global detection problem is to simply increase the number of sensors in the monitored structure by creating dense sensor networks (DSNs). These networks, often termed electronic artificial skins, e-skins or sensing skins, are thin electronic sheets that

* Corresponding author.
E-mail address: adowney2@iastate.edu (A. Downey).

http://dx.doi.org/10.1016/j.jweia.2017.06.016
Received 29 November 2016; Received in revised form 9 May 2017; Accepted 20 June 2017

mimic the ability of biological skin to detect and localize damage. Sensing skins often consist of rigid or semi-rigid cells mounted on a flexible sheet, as demonstrated by Xu et al. (2003) and Lee et al. (2006). Recent developments in sensing skins have progressed towards the development of microelectromechanical systems (MEMS) mounted in flexible sheets without the need for rigid packaging (Mahmood et al., 2015). Sensing skins with the transducing sensor built into the skin have been proposed (Chang et al., 2008). Additionally, Sensing skins with integrated electronics for signal processing have also been introduced (Yao and Glisic, 2015). These integrated sensing skins offer the potential to enable low-cost direct sensing and can be scaled for the monitoring of mesoscale systems, including wind turbine blades. Schulz et al. have proposed the use of a dense sensor network of series-connected piezoceramic (PZT) nodes for the continuous monitoring of wind turbine blades Schulz and Sundaresan (2006). The densest deployment of sensors for the SHM of wind turbine blades known to the authors was done by Rumsey et al. at Sandia National Laboratories Rumsey and Paquette (2008). Various sensor technologies were investigated for the potential of monitoring a composite blade's structural condition during a fatigue test. Generally, successful damage detection was found to require optimal sensor placement, synchronization of sampling between different sensor types, and having sensor technology capable of detecting damage that occurs on a small scale while being able to be distributed as an array over the entire structure.

Leveraging recent advances in the field of flexible electronics (Rogers et al., 2010), the authors have developed a sensing skin termed the soft elastomeric capacitor (SEC). Developed around an inexpensive nanocomposite based on a styrene-co-ethylene-co-butylene-co-styrene (SEBS) block co-polymer, the SEC is a low-cost sensor customizable in shape and size (Laflamme et al., 2013a). Its static (Laflamme et al., 2013b) and dynamic (Laflamme et al., 2015) behaviors have been characterized, including numerical and experimental damage detection applications to wind turbine blades (Laflamme et al., 2016; Downey et al., 2017). Additionally, the effectiveness of a DSN consisting of SECs for detecting fatigue cracks has been demonstrated (Kharroub et al., 2015). A particularity useful attribute of the SEC is its ability to measure additive in-plane strain, and therefore, its signal must be decomposed into orthogonal directions if one desires to reconstruct uni-directional strain maps.

With the advancement of low-cost, high-channel-count sensing skins, damage detection and data-fusion techniques need to be developed to provide SHM and PHM capabilities based on this unique class of sensors. Data fusion consists of the integration of sensor data from a multitude of sources in order to make a useful representation of the monitored systems. This representation should be of sufficient quality to assist in forming a damage detection, localization, and quantification decision. Additionally, data fusion can be used to obtain a damage detection feature from multiple sensors that is informative and non-redundant. In the case of SHM, features should allow for the distinction between a damaged and an undamaged state. Examples found in the literature are most commonly based on measured dynamic signals such as resonant frequencies, mode shapes, or properties derived from mode shapes (Zou et al., 2000; Sohn et al., 2003; Han et al., 2006).

This work introduces a computationally efficient data fusion technique that is capable of monitoring mesoscale structures without associated models or historical datasets. More specifically, the proposed NeRF (Network Reconstruction Feature) algorithm is capable of classifying hybrid dense sensor networks (HDSN) sections into healthy, or containing potential damage. This work uses HDSNs consisting of SECs for covering the large areas of a blade and Fiber Bragg grating (FBG) sensors for the enforcement of boundary conditions along the edges of sections and the separation of monitored sections. The SEC is used throughout this work as a large area electronic strain transducer. However, similarly developed large area electronics optimized for strain measurements could also be used (Yao and Glisic, 2015; Burton et al., 2016).

The NeRF algorithm works through comparing an individual sensor's measured state with the estimated response within an HDSN section. This response is built through assuming a shape function and using the least squares estimator (LSE) to approximate uni-directional strain maps. An error function is introduced, which is defined as the mean square error (MSE) between the sensor's measured and estimated strains. Thereafter, features are defined as the change in error associated with a given increase in the shape function's complexity. This technique fuses the SEC and FBG strain data into a single damage detection feature, providing a simple and robust method for inspecting large numbers of sensors without necessitating complex physical models.

The contributions of this work are three-fold: 1) an algorithm for the development of a damage detection feature that integrates data from a newly proposed HDSN into a single detection value is introduced; 2) a demonstration of the damage detection feature's ability to detect, quantify and localize damage; and 3) the evaluation of the damage detection feature's capabilities without relying on models or historical datasets. This paper is organized as follows. Section 2 introduces the SEC along with relevant background including the strain decomposition algorithm previously developed. Section 3 introduces the NeRF algorithms simulations used for validation. Section 4 presents the numerical models used for the simulations. Section 5 discusses the simulation results. Section 6 concludes the paper.

2. Background

This section provides background on the SEC sensor along with a brief review of the extended LSE algorithm for decomposing the SEC additive in-plane strain signal.

2.1. Soft elastomeric capacitor

The SEC is a thin film, large area sensor that transduces a change in its geometry (i.e., the monitored substrate strain) into a change in capacitance. The SEC measures in-plane strain ($x-y$ plane in Fig. 1(insert)). The fabrication process of the SEC is documented in Laflamme et al. (2013a). Briefly, the dielectric is fabricated from an SEBS block co-polymer filled with titania to enhance its durability and permittivity. The conductive plates are fabricated from an SEBS filled with carbon black particles. The SEC is a highly scalable technology, because it uses only commercially available and inexpensive materials and its

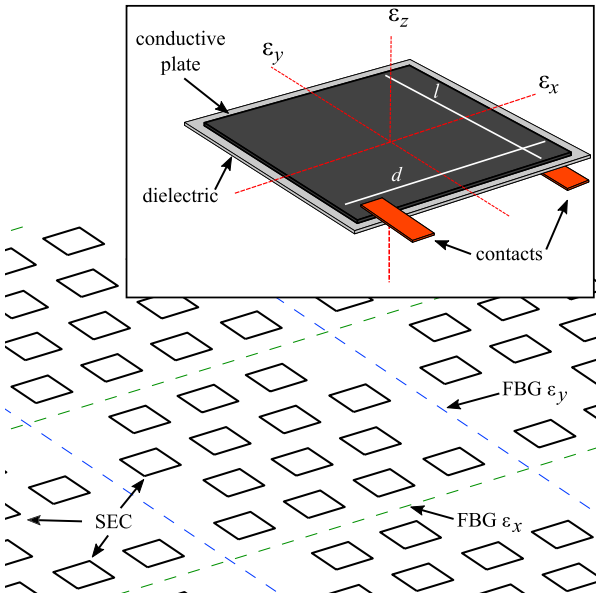

Fig. 1. HDSN technology: HDSN section with FBG sensors enforcing strain boundary conditions and SECs providing large area sensing coverage; insert: annotated SEC sensor with reference axes.

fabrication process is simple.

SECs are adhered to the monitored substrate under pre-stress using a commercial epoxy, allowing it to measure strain under both tension and compression. Its electro-mechanical model is derived in Laflamme et al. (2015). Briefly, assuming a low sampling rate (< 1 kHz), the SEC can be modeled as a non-lossy capacitor with capacitance C, given by the parallel plate capacitor equation,

$$C = e_0 e_r \frac{A}{h} \tag{1}$$

where $e_0 = 8.854$ pF/m is the vacuum permittivity, e_r is the polymer relative permittivity, $A = d{\cdot}l$ is the overlapping area of the conductive electrodes and h is the thickness of the dielectric.

Assuming small in-plane strain, an expression relating the sensor's change in capacitance to the substrate's surface strain can be expressed as

$$\frac{\Delta C}{C} = \lambda(\varepsilon_x + \varepsilon_y) \tag{2}$$

where $\lambda = 1/(1-\nu)$ represents the gauge factor of the sensor. For SEBS, $\nu \approx 0.49$, which yields a gauge factor $\lambda \approx 2$. Eq. (2) shows that the signal of the SEC varies as a function of the orthogonal strain components $\varepsilon_x + \varepsilon_y$. The linearity of the electro-mechanical model has been validated for mechanical responses under 15 Hz (Laflamme et al., 2015). For mechanical responses up to 40 Hz, an altered electro-mechanical model is presented in Saleem et al. (2015) but is not shown here for brevity. The SEC's electro-mechanical model has been validated for both static and dynamic strain and is presented in references (Laflamme et al., 2013a, 2015; Saleem et al., 2015).

2.2. Strain decomposition algorithm

Leveraging an HDSN configuration, orthogonal strain maps can be obtained from the additive strain measured by the SEC, as expressed in Eq. (2), using a network of sensors in combination with boundary conditions enforced using linear strain measurement techniques. In this work, FBG sensors are used as linear strain sensors. These measurements are used for updating the HDSN at key locations. The algorithm, termed the extended LSE algorithm, is presented in Downey et al. (2016) and summarized in what follows.

The extended LSE algorithm starts by assuming a parametric displacement shape function. Here, a p^{th} order polynomial is selected as the displacement shape function due to its mathematical simplicity and its capability to develop a wide range of displacement topographies. The shape function is developed for the x-y plane with a constant plate thickness c, such that the deflection shape w is expressed as

$$w(x,y) = \sum_{i=1,j=1}^{p} b_{ij} x^i y^j \tag{3}$$

where $b_{i,j}$ are regression coefficients. Considering an HDSN with m sensors that includes both SEC and FBG sensor nodes, and collecting displacements at sensor locations in a vector $\mathbf{W} \in \mathbb{R}^m$, Eq. (3) becomes $\mathbf{W} = \begin{bmatrix} w_1 & \cdots & w_k & \cdots & w_m \end{bmatrix}^T = \mathbf{HB}$. Here, $\mathbf{H}$ encodes information on sensor locations and $\mathbf{B}$ contains the regression coefficients such that $\mathbf{B} = \begin{bmatrix} b_1 & \cdots & b_f \end{bmatrix}^T$ where b_f represents the last regression coefficient.

Appropriately defined diagonal weight matrices $\mathbf{\Gamma}$ are introduced into the $\mathbf{H}$ matrix to account for the SEC additive strain measurements such that $\mathbf{H}$ is defined as $\mathbf{H} = [\mathbf{\Gamma}_x \mathbf{H}_x | \mathbf{\Gamma}_y \mathbf{H}_y]$. $\mathbf{\Gamma}_x$ and $\mathbf{\Gamma}_y$ hold sensor weight values along the x and y axes, respectively. These matrices are formed with scalars $\gamma_{x,k}$ and $\gamma_{y,k}$ associated with the k-th sensor. For instance, an FBG node k oriented to make strain measurements in the x direction will take weight values $\gamma_{x,k} = 1$ and $\gamma_{y,k} = 0$. The following matrices are developed from quantities contained in (3):

$$\mathbf{H}_x = \mathbf{H}_y = \begin{bmatrix} y_1^n & x_1 y_1^{n-1} & \cdots & x_1^{n-1} y_1 & x_1^n \\ y_m^n & x_m y_m^{n-1} & \cdots & x_m^{n-1} y_m & x_m^n \end{bmatrix} \tag{4}$$

Linear strain functions ε_x and ε_y along the x and y directions, respectively, can be obtained from Eq. (3) through the enforcement of Kirchhoff's plate theory as

$$\varepsilon_x(x,y) = -\frac{c}{2}\frac{\partial^2 w(x,y)}{\partial x^2} = \mathbf{\Gamma}_x \mathbf{H}_x \mathbf{B}_x \tag{5}$$

$$\varepsilon_y(x,y) = -\frac{c}{2}\frac{\partial^2 w(x,y)}{\partial y^2} = \mathbf{\Gamma}_y \mathbf{H}_y \mathbf{B}_y \tag{6}$$

where $\mathbf{B} = [\mathbf{B}_x | \mathbf{B}_y]^T$.

Constructing a signal vector, $\mathbf{S} = \begin{bmatrix} s_1 & \cdots & s_k & \cdots & s_m \end{bmatrix}^T$ where $\mathbf{S}$ contains the additive SEC and unidirectional FBG strain measurements, the regression coefficient matrix $\mathbf{B}$ can be estimated using an LSE:

$$\widehat{\mathbf{B}} = (\mathbf{H}^T\mathbf{H})^{-1}\mathbf{H}^T\mathbf{S} \tag{7}$$

where the hat denotes an estimation. Estimated strain maps can now be reconstructed using

$$\widehat{\mathbf{E}}_x = \mathbf{\Gamma}_x \mathbf{H}_x \widehat{\mathbf{B}}_x \quad \widehat{\mathbf{E}}_y = \mathbf{\Gamma}_y \mathbf{H}_y \widehat{\mathbf{B}}_y \tag{8}$$

where $\widehat{\mathbf{E}}_x$ and $\widehat{\mathbf{E}}_y$ are vectors containing the estimated strain in the x and y directions, respectively.

In the case of an HDSN without a sufficient number of unidirectional inputs, $\mathbf{H}$ will be multi-collinear as $\mathbf{H}_x$ and $\mathbf{H}_y$ will share multiple rows, resulting in $\mathbf{H}^T\mathbf{H}$ being non-invertible. Additionally, $\mathbf{H}^T\mathbf{H}$ may lack sufficient information to be invertible for a shape function of high complexity. It follows that $\mathbf{H}^T\mathbf{H}$ is invertible given a sufficient level of input information for a given shape function. Experimental validation of the extended LSE algorithm for static Downey et al. (2016) and dynamic conditions Downey et al. (2017) have been used to validate the strain decomposition method in field conditions.

3. NeRF algorithm

The proposed NeRF algorithm is presented in what follows.

3.1. Network reconstruction feature (NeRF)

The algorithm provides damage detection and localization capabilities by subdividing a complex geometry into a set of geometrically smaller, and typically simpler, sections. The algorithm works by comparing the signal measured by an individual sensor with the estimated response within a predefined HDSN section. The estimated response is obtained by assuming a shape function and using a least squares estimator (LSE) to approximate uni-directional strain maps. An error function, defined as the mean square error (MSE) between a sensor's measured and estimated strains, is used to associate a feature value with a given increase in the shape function complexity. An advantage is that the HDSN can be strategically customized (e.g., to monitor crack growth, or inspect a key structural location). Fig. 2 illustrates this idea where a high-resolution HDSN is deployed inside a wind turbine blade along the leading edge where the geometry is more complex, and a low-resolution HDSN is deployed inside the blade along the trailing edge of the blade where the geometry is simpler.

Consider an HDSN section similar to that shown in Fig. 2, consisting of optical fibers with integrated FBG sensors forming the perimeter and SECs placed within. Establishing the NeRF's theoretical foundation requires that we first consider an ideal situation where strain maps are easily approximated through the use of low order shape functions. The error in the approximation, calculated for m sensors, can be quantified as:

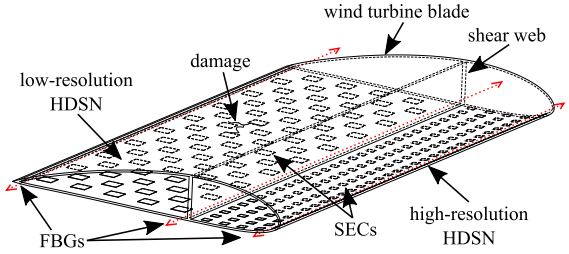

Fig. 2. Subdividing a wind turbine blades' complex geometry into independent sections of different resolutions, here the HDSN is deployed only along the bottom of the wind turbine blade for clarity.

$$V = \frac{1}{m}\sum_{k=1}^{m}\left(S_k - S_k'\right)^2 \tag{9}$$

where V is the MSE value. For a given sensor location k, S_k is the sensor signal, and S_k' is the estimated sensor signal using the reconstructed strain maps. The estimated sensor signals for FBG sensors measuring ε_x and ε_y are taken from $\widehat{\mathbf{E}}_x$ and $\widehat{\mathbf{E}}_y$, respectively, while the estimated SEC signals are taken as the summation of $\widehat{\mathbf{E}}_x$ and $\widehat{\mathbf{E}}_y$ at any given location (Eq. (2)). The algorithm is outlined in Fig. 3 where orthogonal strain maps are created using the extended LSE algorithm shown inside the red dashed rectangle.

Generally, undamaged structural components will result in strain fields with relatively simple topologies that can be estimated with low-order shape functions. Adding damages into the monitored substrate will produce highly curved strain fields that require higher-order shape functions to reconstruct to the same level of reconstruction error. This principle is leveraged in the proposed method for damage detection and localization. The proposed NeRF algorithm monitors a section's reconstruction error (V) in response to adding higher order shape functions. As the higher-order terms are added to the shape function, the reconstruction error (V) between the estimated and measured state will substantially reduce in the case of damaged sections. Therefore, the condition of a section can be assessed from the changing level of reconstruction error. This technique provides damage detection potential within the monitored area, even at locations that are not directly covered by an SEC. This technique adds versatility to the proposed HDSN for monitoring meso-scale structures such as wind turbine blades, by reducing the number and density of required sensors.

3.2. Feature extraction

Starting with $w(x, y) = \sum_{i=1,j=1}^{2} b_{ij}x^i y^j$, the binomial terms listed in Table 1 are shape function components that are added in symmetric pairs from the outside of the Pascal triangle propagating inwards for a given row. Therefore, value for feature No. 1 becomes the difference in reconstruction error, **V**, between the baseline shape function $w(x, y) = \sum_{i=1,j=1}^{2} b_{ij}x^i y^j$ and the baseline shape function with term No. 1 added $w(x, y) = \sum_{i=1,j=1}^{2} b_{ij}x^i y^j + x^3 + y^3$. Similarly, feature No. 2 becomes the difference between $w(x, y) = \sum_{i=1,j=1}^{2} b_{ij}x^i y^j + x^3 + y^3$ and $w(x, y) = \sum_{i=1,j=1}^{2} b_{ij}x^i y^j + x^3 + y^3 + x^2y + xy^2$, and so forth. Note that no

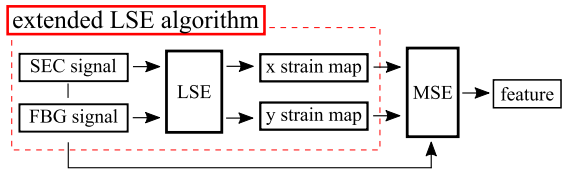

Fig. 3. Network reconstruction feature (NeRF) algorithm.

Table 1
Polynomial complexities used for condition assessment features.

No.	term added	No.	term added
1	x^3, y^3	8	x^3y^2, x^2y^3
2	x^2y, xy^2	9	x^6, y^6
3	x^4, y^4	10	x^5y, xy^5
4	x^3y, xy^3	11	x^7, y^7
5	x^2y^2	12	x^6y, xy^6
6	x^5, y^5	13	x^5y^2, x^2y^5
7	x^4y, xy^4	14	x^4y^3, x^3y^4

displacement-defined boundary conditions are enforced into the shape functions. Instead, all boundary conditions are enforced into strain topography through the use of the uni-directional FBG sensors. The development of features from each HDSN section provides a high level of data compression from the fusion of all sensor signals **S** into a single feature-based scalar.

4. Numerical models

The proposed NeRF algorithm is validated on two different numerical models intended as a preliminary validation to demonstrate the concept of the proposed algorithm. In this regards, it is worth commenting that real wind turbine blades are complex composite layups, representing highly optimized structures with complicated aerodynamic shapes Wang et al. (2016); Malcolm and Hansen (2002), under highly varying loading conditions and exhibiting various failure conditions Kong et al. (2005); Rumsey and Paquette (2008). Therefore, the selected models are to demonstrate the theory associated with the proposed algorithm and should not be considered as accurate representations of a full-scale wind turbine blade. The conclusive validation of the proposed algorithm would therefore require experimental or field tests that go beyond the purposes of this work.

For each presented model, the HDSN sections are constructed similarly to the configuration illustrated in Fig. 1, where networks of SEC sections are divided by FBG sensors measuring either ε_x or ε_y. SECs are placed on an offset grid to allow for more complete coverage, and to introduce some complexity into $\mathbf{H}^T\mathbf{H}$ following preliminary results suggesting that this configuration may increase the HDSN's capability to detect damage that is not directly monitored by an SEC. Sensors are positioned with a slight randomness of ±2 cm to account for simulated error in placement and to add a small amount of non-uniformity to the HDSN sections to better approximate an installed condition. FBGs are placed along the x and y axes with a small gap around the edge to reproduce a realistic installation. Gaussian noise is introduced into the sensors signals with noise levels of 25±$\mu\varepsilon$ for the SECs (taken from previous work (Laflamme et al., 2013b)) and ±5 $\mu\varepsilon$ for the FBG nodes, representing a typical FBG systems with low-resolution (Majumder et al., 2008).

The first simulated model is a cantilever beam under uniform tensional loading of 45 kN/m, as shown in Fig. 4(a). It is used to validate the NeRF algorithm under simple geometry and loading. The HDSN sections are constructed with networks of 14 SECs, as denoted by the number in the bottom right corner of each section, divided by unbroken strands of continuous optical fibers with integrated FBG sensors measuring either ε_x or ε_y. Three damage cases are used (illustrated in Fig. 4(a) as I, II, and III), each to investigate particular opportunities and limitations of the NeRF: case I) capacity to detect and quantify large damage in an area where the strain field has relatively small curvatures; case II) capacity to detect large damage spanning two HDSN sections; and case III) capacity to detect small damage in an area of relatively complex strain maps. Damage is introduced in the form of composite ply delamination and is represented into the model by a 50% reduction in stiffness for the affected area Rodriguez (2016). A stiffness reduction of 25% was also introduced for damage case I to determine the ability of the NeRF

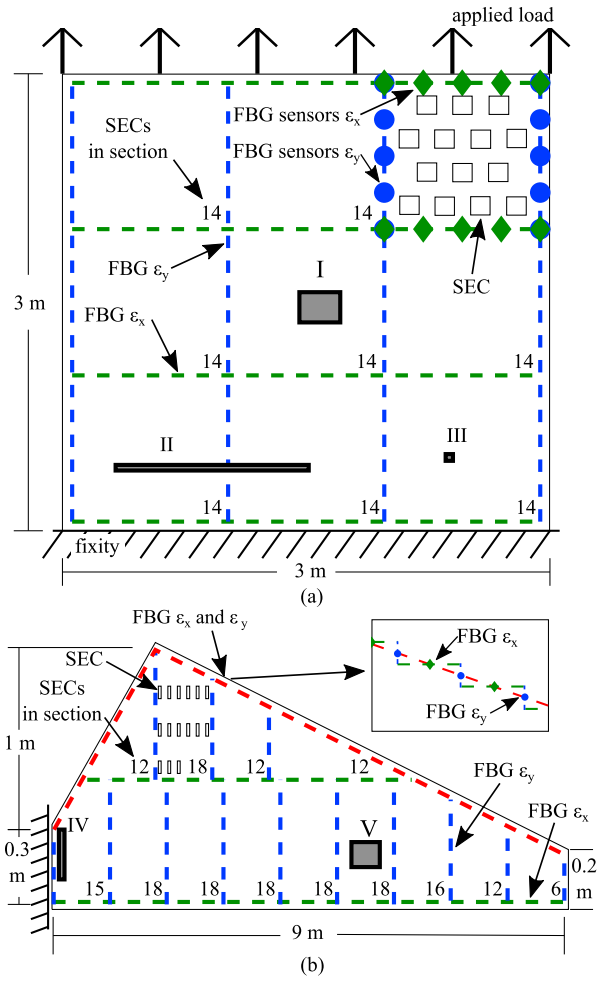

Fig. 4. HDSNs used in simulation of the NeRF: a) rectangular cantilever plate under tensile loading; and b) wind turbine shaped cantilever plate under pressure loading; insert: routing of FBG over diagonal edge to provide alternating measurements of ε_x and ε_y.

algorithm to quantify the extent of the damage.

The second simulated model is a wind turbine blade simplified as an isotropic cantilever plate (Rumsey and Paquette, 2008) illustrated in Fig. 4(b). A uniform pressure load of 1 kN/m^2 is applied onto the top surface of the model. Similarly to the first simulated model, the HDSN sections are constructed with network grids of SECs divided by unbroken strands of continuous FBG sensors. In the case of FBG sensor along the diagonal edge of the blade, the FBG sensors are arranged as shown in the insert of Fig. 4(b) to provide alternating ε_x or ε_y signals along the diagonal. The number of SECs per section is denoted in the lower right corner of each section. This configuration is used to assess two additional opportunities and limitations: case IV) capacity to detect damage present in locations of highly curved strain fields; and case V) capacity to detect damage present in areas of low curvature strain fields relatively close to instances of more complex strain fields. Table 2 lists model-specific data relating to both finite element models and their corresponding HDSN. For both models, a mesh convergence study was performed. The sizes of mesh were selected to ensure that each model had a dense enough meshing to allow each simulated SEC to cover at least six elements.

Table 2
HDSN and FEA configurations.

	model 1	model 2
	rectangle	blade
HDSN sections	9	13
SECs	126	194
SEC size	120 cm^2	120 cm^2
FBG points	104	249
FBG points (x)	52	141
FBG points (y)	52	108
FEA elements	shell	shell
No. of elements	25,372	52,590
No. of integration points	9	9
Young's Moduli	20 GPa	20 GPa
Density	2 kg/mL	2 kg/mL
Loading	45 kN/m	1 kN/m^2
Thickness	7 mm	40 mm

5. Results

This section presents and discusses simulation results for the validation of the NeRF algorithm. Feature extraction and quantification for an example damage case is first demonstrated. It is followed by a presentation of data for each damage case, and a discussion of the algorithm's performance at damage localization.

5.1. NeRF features

Consider the HDSN that contains damage case I. The level of sensor error V obtained as a function of the increasing shape function complexity is shown in Fig. 5, where its mean sensor error (V) and the individual reconstruction errors are plotted for the healthy case (Fig. 5(a)) and for the damage case I (Fig. 5(b)). Here, polynomial complexity 0 reports V when using the shape function , $w(x, y) = \sum_{i=1,j=1}^{2} b_{ij} x^i y^j$ with each corresponding term being added sequentially. The corresponding features, quantified as the reduction in error (ε^2) between two polynomial complexity terms are presented along the bottom of the plots. Feature numbering is related to the higher order term used in constructing the feature. The scatter for the polynomial complexities is a result of noise introduced into the sensors.

The healthy state, as shown in Fig. 5(a), converges after a few added shape function terms, demonstrating that the strain topography can be easily reproduced with a relatively simple shape function. This is demonstrated by the fact that adding more complex terms to the shape

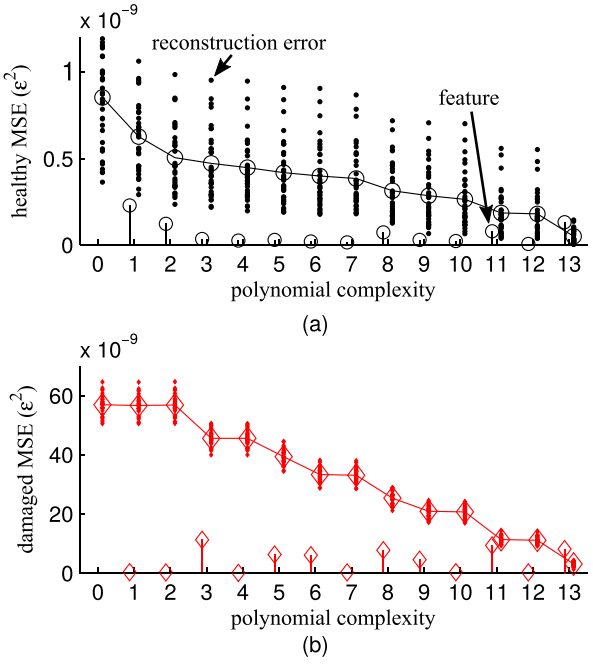

Fig. 5. Reconstruction error **V** (scatter plot) and extracted corresponding features (stem plot along the bottom) for the HDSN containing damage case I: a) healthy state; b) damage state (damage case I).

function results in only incremental improvements. In comparison, damage case I starts with a considerably higher level of strain error and continuously benefits from adding more complexity to the shape functions. In both cases, the shape function beyond that produced by term No. 13 became overly complex, whereas $\mathbf{H}^T\mathbf{H}$ becomes non-invertible. Therefore, solving for higher shape function with greater complexity would require additional sensors be added into the HDSN section. As expected, the feature values are greater for the damaged case when compared to the healthy state, providing a means to detect and quantify damage.

5.2. Damage quantification

The magnitude of features can be used to quantify different levels of damage as presented in Fig. 6. Here, features obtained from adding polynomial complexities terms No. 3 and 13 are used to distinguish varying levels of damage for damage case I. Damage levels in the form of a reduction in stiffness of 25% and 50% for the damaged area are shown. Each feature scatter increases as the damage level increases. This is as expected given that the LSE encounters more variation with the increase in topology complexity. The feature distance can be calculated as any n-dimensional combination of NeRF features. A two-dimensional feature taken from the mean of the distances is shown here for simplicity. A two-dimensional Gaussian distribution confidence interval with amplitude 2σ, where σ is the standard deviation, is plotted over the scatter plot to show the distribution of features.

5.3. Damage localization

Damage localization can be conducted through the spatial comparison of feature values or feature distances taken as the Euclidean distance between the origin and the center of a Gaussian cluster such as that illustrated in Fig. 6. Results shown in Fig. 7 are taken as the feature distance from the center points of features No. 6, 9, and 11, and the origin. First, the simple cantilever plate under a tension load is considered. Fig. 7(a) presents the healthy state of the plate while Fig. 7(b–d) present damage cases I to III, respectively. As expected, Fig. 7(a) shows that a more complex strain topology is located at the fixity of the plate. These results are to be expected as the fixity will result in more complex local strain fields. The non-symmetric relationship is most likely a result of the slight randomness applied to individual SEC layouts, resulting in non-identical HDSN sections, and of the noise induced into the sensor signals. Damage case I is presented in Fig. 7(b). Here, the location of a high strain map reconstruction error V is easily detectable as the error caused by the damage case is significantly higher than that present along the fixed edge. This sharp increase in error demonstrates the capability of the NeRF algorithm to distinguish between HDSNs that may be damaged

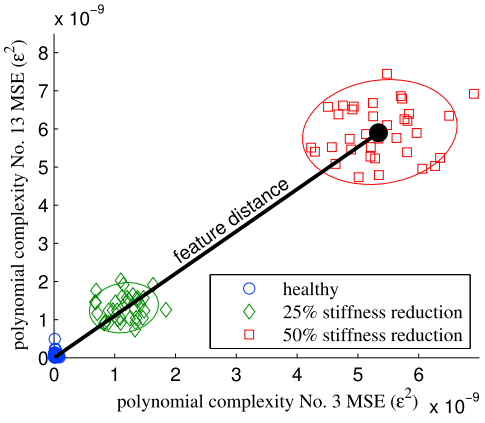

Fig. 6. Feature distance for complexities terms No. 3 and 13 showing results for varying levels of damage.

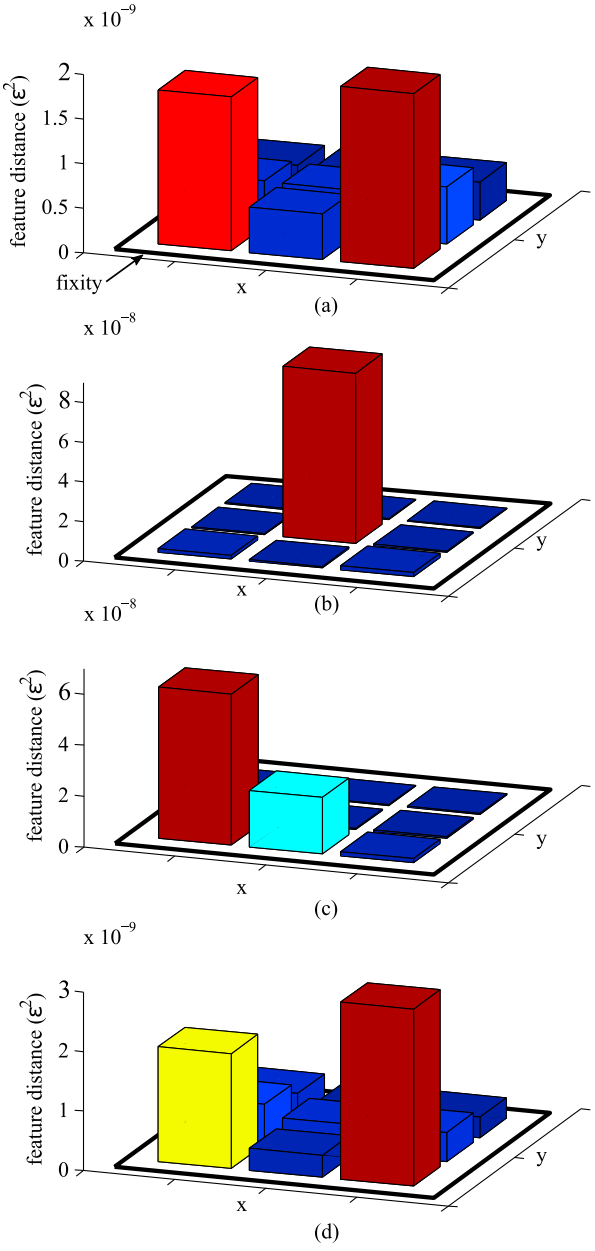

Fig. 7. Damage detection and localization for the square plate using feature distances: a) healthy case; b) damage case I; c) damage case II; and d) damage case III.

from those that are healthy. This damage case is detectable without the use of historical data or external models.

Damage case II is introduced to test the NeRF algorithm's robustness to multiple damaged sections, here placed across two HDSN sections (illustrated in Fig. 4(a)). The feature distance results, presented in Fig. 7(c) demonstrate that the algorithm is capable of detecting damage in both HDSN sections. These results provide evidence that the NeRF algorithm is robust in terms damage detection across multiple HDSN sections, allowing greater flexibility in terms of HDSN layout.

Damage case III is used to study the algorithm's capability to detect a small damage not directly measured by any SEC sensor, as shown in Fig. 8(a). Damage case III consists of a 50% reduction in stiffness for a 0.2% area of the HDSN section, positioned between SEC sensors. Feature distances are presented in Fig. 7(d). While the magnitude of the feature distance increased by approximately 50%, form 1.95×10^{-9} (ε^2) for the healthy state to 2.97×10^{-9} (ε^2) for the damaged state, the assessment of damage is difficult because a complex strain topology is already present

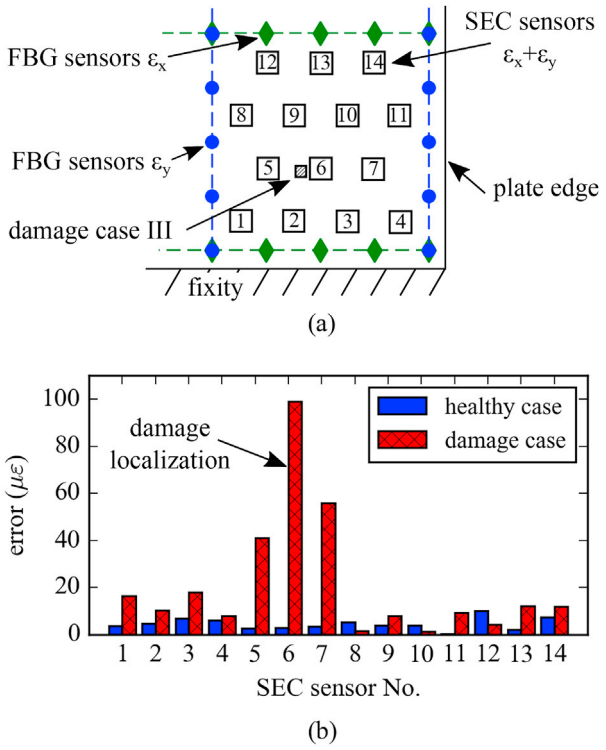

Fig. 8. Damage localization within an HDSN: a) damage case III and associated HDSN; b) absolute difference (error) between the estimated and measured strain for SECs within the HDSN.

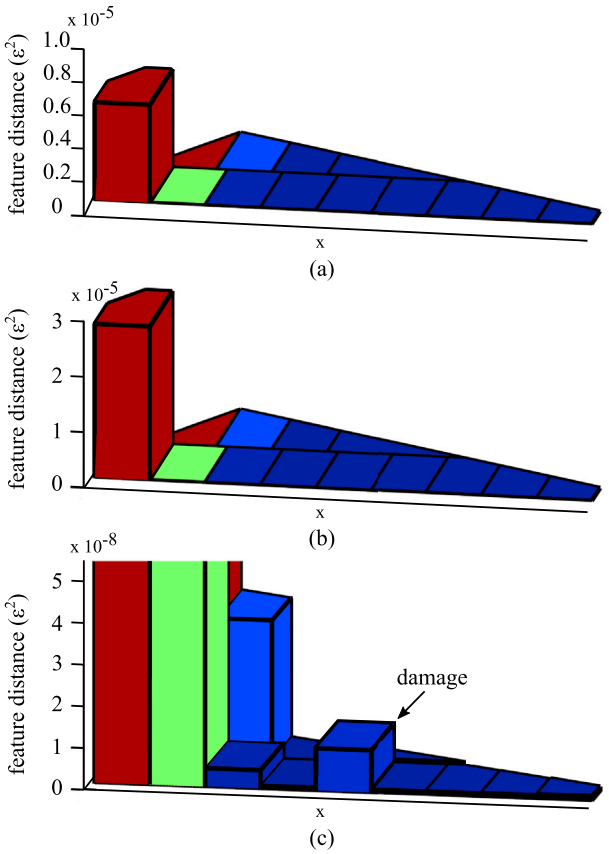

Fig. 9. Damage detection for wind turbine blade using feature distances: a) healthy case; b) damage case IV; and c) damage case V.

in the HDSN section of interest. An alternative is to compare the measured strain with the estimated strain for individual sensors throughout the HDSN.

To do so, the estimated strain for the damaged and undamaged case is obtained using the extended LSE algorithm and a high order shape function encompassing complexity terms 0–11 for the HDSN section of interest. The high complexity shape function, using complexity terms 0–11 was selected to match the highest polynomial complexity term used in building the damage feature distance and is capable of developing accurately reconstructed strain maps for the HDSN section. Fig. 8(b) shows the absolute error between the additive SEC sensor signal and the reconstructed strain maps for both the healthy and damaged states. Note that for the healthy case, the error is relatively small for all SEC sensors. When damage is introduced into the HDSN section the mean error of the section increases. The damage can easily be localized as close to SEC No. 6 due to the high strain difference between the estimated and measured strain of 98 $\mu\varepsilon$. Sensors No. 5 and 7 also show a large error value for the damage case III where sensor No. 7 is higher due to the more complex strain topography in that section of the HDSN. All other SEC error values fall within strain difference of 20 $\mu\varepsilon$ and therefore fall close to the system's noise band. A reduction in system noise or filtering of sensor signals is required for localizing damage with respect to other sensors (e.g. SEC No. 9 and 2). These findings demonstrate that the NeRF algorithm is capable of detecting and localizing relativity small damage within an HDSN, using only sensor data without any external models or assumptions.

To further investigate the performance of the NeRF algorithm, two additional damage cases are studied on the more complex wind turbine blade model presented in Fig. 4(b). Results are presented in Fig. 9 in the same format as for Fig. 7, using the Euclidean distance computed between the center of feature clusters No. 6, 9 and 11, and the origin. Fig. 9(a) presents the healthy state of the wind turbine blade, with highly complex strain topology located at the base (root) of the cantilever plate, as expected. The HDSN section at the root experiences high levels of strain and torsion due to the loading and asymmetric shape of the blade. Damage case IV is introduced into this section and results are illustrated in Fig. 9(b). The introduction of damage greatly increases the strain topology of the HDSN, even considering its previous complexity. Results demonstrate that the feature distance increased from 0.62×10^{-5} (ε^2) to 2.95×10^{-5} (ε^2). The increase in feature distance is significant and similar to damage case III in that an external model or historical data would need to be applied to detect damage because of the complex strain topology already present in the HDSN section. However, similar to damage case III the damage can be localized withing the HDSN section of interest as presented in Fig. 10. Again, Fig. 10(a) shows the location of the damage case and Fig. 10(b) presents the absolute error in the strain data between the measured state and the reconstructed strain fields for the SEC sensors in the HDSN of interest. For compatibility with results presented before, a shape function using complexity terms 0–11 was used to reconstruct the global strain maps. Here, damage can be localized though comparing error in the damage case for SEC sensors 1,2,7 and 8 to their respective healthy state. These results further strengthen the localization results found for damage case III. In contrast to damage case IV, damage case V presented in Fig. 9(c) exhibits a situation where damage is detectable through comparison with neighboring sections.

Simulation results demonstrate that an HDSN using NeRF is capable of damage detection, quantification, and localization. The input load used here is static and similar across cases with only sensor noise being considered. In situations where dynamic loading is relatively constant, such as a wind turbine blade in operation, a set of sample measurement could be taken at a reoccurring interval such as when a blade is in the vertical position providing a semi-constant loading reference. Furthermore, an average of samples taken continuously over several revolutions could be used to build the NeRF features, assuming that the average load

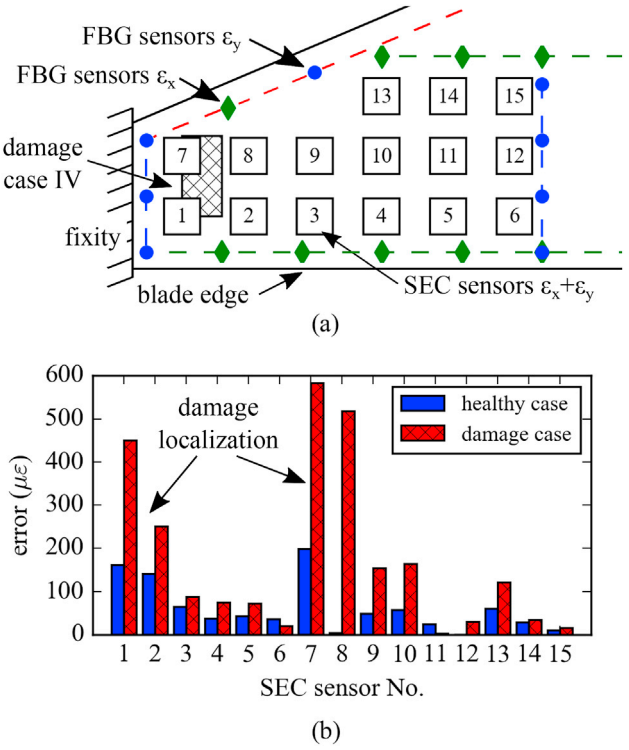

Fig. 10. Damage localization within an HDSN: a) damage case IV and associated HDSN; b) absolute difference (error) between the estimated and measured strain for SECs within the HDSN.

is relatively constant over a period of time.

Damage detection and localization performance may be improved through the deployment of denser, more complex HDSNs in areas where greater strain topologies are present. NeRF is also capable of providing a high level of data compression in the form of features fused from sections of an HDSN. Take for example the cantilever plate model. The feature distance calculated for each HDSN section is the result of the fusion of 34 individual data channels, when extended to the entire plate algorithm provides a data compression of 246 data points to 9, equivalent to a 96.4% data reduction. The blade model represents similar results, providing data compression from 443 data points to 13, equivalent to a 97.0% reduction. Compression of data allows for faster post-processing, retention of longer historical datasets, and a reduction in the cost associated with building prognostic datasets.

6. Conclusion

A computationally efficient, data-driven damage detection, quantification and localization technique was presented for use with hybrid dense sensor networks (HDSN). This method was designed to enable monitoring of mesoscale structures, including wind turbine blades, without associated models or historical datasets. Termed the network reconstruction feature (NeRF), the algorithm allows for the separation of healthy and potentially damaged sections within an HDSN. NeRF fuses high channel count data found in an HDSN to scalar damage detection features. This provides a high level of data compression when implemented over a larger HDSN section. The NeRF algorithm works through first assuming a shape function within an HDSN section and using the least squares estimator (LSE) to approximate uni-directional strain maps within an HDSN section. An error function, defined as the mean square error (MSE) between the sensors' measured and estimated strain is then obtained. Features are defined as the change in error associated with a given increase in the shape function complexity used in the reconstruction of strain maps.

Numerical investigations were conducted to evaluate the performance of NeRF. First, a rectangular cantilever plate was considered, equipped with an HDSN consisting of 126 soft elastomeric capacitors (SEC) and 104 fiber Bragg grating (FBG) nodes, sectioned into nine discrete sections. The NeRF algorithm successfully distinguished between damaged and healthy HDSN sections for all three different damage cases. In the first two damage cases, it was possible to distinguish between healthy and damaged conditions using the Euclidean distance between damage features. The third damage case was difficult to detect by using this strategy because it was highly localized within a region of high strain complexity. Instead, its localization was made possible by comparing the measured strain to the strain estimated using a complex shape function to produce a strain error for each sensor. The damage was then located as being close to the sensors that reported the highest error value. Two additional damage cases were investigated on a more complex shape consisting of a wind turbine blade modeled as a cantilever plate. This second set of simulations confirmed results obtained on the rectangular plate. Lastly, the damage case within the HDSN at the root was localized by comparing the error between the measured strain and the estimated strain. Further collaborating the damage localization results found in the simple plate on a more complex strain topography.

Future investigations are needed to validate the algorithm for use with an extended library of loadings and damage cases, more realistically representing a large wind turbine blade in an operational environment including dynamic loading cases. Sensor network design and partitions, including the number and of SECs within HDSN sections, also needs exploration. The ability of denser networks in regions of highly complex strain maps needs to be studied. This includes the use of asymmetric sensor networks and the inclusion of SECs of different geometries.

Results presented in this paper show that data compression provided by the NeRF algorithm reduces the computational effort and storage space needed to develop and monitor prognostic datasets for large-scale structures. They also demonstrated the promise of the technology at monitoring large-scale surfaces such as wind turbine blades by leveraging a hybrid sensor network configuration. For example, the HDSN combined with the NeRF algorithm could be used to formulate prognostic datasets to detect changes in structural health over time, reducing wind turbines operational cost through the use of damage mitigation technology and real-time structural health management.

Acknowledgments

This work is supported by the National Science Foundation Grant No. 1069283, which supports the activities of the Integrative Graduate Education and Research Traineeship (IGERT) in Wind Energy Science, Engineering and Policy (WESEP) at Iowa State University. Their support is gratefully acknowledged.

References

Afanasyeva, S., Saari, J., Kalkofen, M., Partanen, J., Pyrhönen, O., 2016. Technical, economic and uncertainty modelling of a wind farm project. Energy Convers. Manag. 107, 22–33. http://dx.doi.org/10.1016/j.enconman.2015.09.048.

Borenstein, S., 2012. The private and public economics of renewable electricity generation. J. Econ. Perspect. 26, 67–92. http://dx.doi.org/10.1257/jep.26.1.67.

Burton, A.R., Kurata, M., Nishino, H., Lynch, J.P., 2016. Fully integrated patterned carbon nanotube strain sensors on flexible sensing skin substrates for structural health monitoring. In: Lynch, J.P. (Ed.), Sensors and Smart Structures Technologies for Civil, Mechanical, and Aerospace Systems 2016, SPIE. http://dx.doi.org/10.1117/12.2222501.

Celik, A.N., 2003. Energy output estimation for small-scale wind power generators using weibull-representative wind data. J. Wind Eng. Ind. Aerodynam. 91, 693–707. http://dx.doi.org/10.1016/s0167-6105(02)00471-3.

Chang, N.K., Su, C.C., Chang, S.H., 2008. Fabrication of single-walled carbon nanotube flexible strain sensors with high sensitivity. Appl. Phys. Lett. 92, 063501. http://dx.doi.org/10.1063/1.2841669.

Cockerill, T., Kühn, M., van Bussel, G., Bierbooms, W., Harrison, R., 2001. Combined technical and economic evaluation of the northern european offshore wind resource. J. Wind Eng. Ind. Aerodynam. 89, 689–711. http://dx.doi.org/10.1016/s0167-6105(01)00066-6.

Downey, A., Laflamme, S., Ubertini, F., 2016. Reconstruction of in-plane strain maps using hybrid dense sensor network composed of sensing skin. Meas. Sci. Technol. 27, 124016. http://dx.doi.org/10.1088/0957-0233/27/12/124016.

Downey, A., Laflamme, S., Ubertini, F., Sarkar, P., 2017. Experimental Damage Detection of Wind Turbine Blade Using Thin Film Sensor Array. http://dx.doi.org/10.1117/12.2261531.

Ekelund, T., 2000. Yaw control for reduction of structural dynamic loads in wind turbines. J. Wind Eng. Ind. Aerodynam. 85, 241–262. http://dx.doi.org/10.1016/s0167-6105(99)00128-2. URL:

Ghoshal, A., Sundaresan, M.J., Schulz, M.J., Pai, P.F., 2000. Structural health monitoring techniques for wind turbine blades. J. Wind Eng. Ind. Aerodynam. 85, 309–324. http://dx.doi.org/10.1016/s0167-6105(99)00132-4.

Gross, E., Zadoks, R., Simmermacher, T., Rumsey, M., 1999. Application of damage detection techniques using wind turbine modal data. In: 37th Aerospace Sciences Meeting and Exhibit, American Institute of Aeronautics and Astronautics. http://dx.doi.org/10.2514/6.1999-47.

Han, T., Yang, B.S., Choi, W.H., Kim, J.S., 2006. Fault diagnosis system of induction motors based on neural network and genetic algorithm using stator current signals. Int. J. Rotating Mach. 2006, 1–13. http://dx.doi.org/10.1155/ijrm/2006/61690.

Kharroub, S., Laflamme, S., Song, C., Qiao, D., Phares, B., Li, J., 2015. Smart sensing skin for detection and localization of fatigue cracks. Smart Mater. Struct. 24, 065004. http://dx.doi.org/10.1088/0964-1726/24/6/065004.

Kong, C., Bang, J., Sugiyama, Y., 2005. Structural investigation of composite wind turbine blade considering various load cases and fatigue life. Energy 30, 2101–2114. http://dx.doi.org/10.1016/j.energy.2004.08.016.

Laflamme, S., Cao, L., Chatzi, E., Ubertini, F., 2016. Damage detection and localization from dense network of strain sensors. Shock Vib. 2016, 1–13. http://dx.doi.org/10.1155/2016/2562949.

Laflamme, S., Kollosche, M., Connor, J.J., Kofod, G., 2013a. Robust flexible capacitive surface sensor for structural health monitoring applications. J. Eng. Mech. 139, 879–885. http://dx.doi.org/10.1061/(asce)em.1943-7889.0000530.

Laflamme, S., Saleem, H.S., Vasan, B.K., Geiger, R.L., Chen, D., Kessler, M.R., Rajan, K., 2013b. Soft elastomeric capacitor network for strain sensing over large surfaces. IEEE/ASME Trans. Mechatron. 18, 1647–1654. http://dx.doi.org/10.1109/tmech.2013.2283365.

Laflamme, S., Ubertini, F., Saleem, H., D'Alessandro, A., Downey, A., Ceylan, H., Materazzi, A.L., 2015. Dynamic characterization of a soft elastomeric capacitor for structural health monitoring. J. Struct. Eng. 141, 04014186. http://dx.doi.org/10.1061/(asce)st.1943-541x.0001151.

Lee, H.K., Chang, S.I., Yoon, E., 2006. A flexible polymer tactile sensor: fabrication and modular expandability for large area deployment. J. Microelectromec. Syst. 15, 1681–1686. http://dx.doi.org/10.1109/jmems.2006.886021.

Mahmood, M.S., Celik-Butler, Z., Butler, D.P., 2015. Design and Fabrication of Self-packaged, Flexible MEMS Accelerometer. In: 2015 IEEE Sensors. IEEE. http://dx.doi.org/10.1109/icsens.2015.7370305.

Majumder, M., Gangopadhyay, T.K., Chakraborty, A.K., Dasgupta, K., Bhattacharya, D., 2008. Fibre bragg gratings in structural health monitoring—present status and applications. Sens. Actuators A Phys. 147, 150–164. http://dx.doi.org/10.1016/j.sna.2008.04.008.

Malcolm, D., Hansen, A., 2002. Windpact Turbine Rotor Design Study. National Renewable Energy Laboratory. Golden, CO 5. URL. http://www.nrel.gov/docs/fy06osti/32495.pdf.

Richards, P.W., Griffth, D.T., Hodges, D.H., 2015. Smart loads management for damaged offshore wind turbine blades. Wind Eng. 39, 419–436. http://dx.doi.org/10.1260/0309-524x.39.4.419.

Rodriguez, G., 2016. Finite Element Modeling of Delamination Damage in Carbon Fiber Laminates Subject to Low-velocity Impact and Comparison with Experimental Impact Tests Using Nondestructive Vibrothermography Evaluation (Ph.D. thesis). California Polytechnic State University, San Luis Obispo. http://digitalcommons.calpoly.edu/cgi/viewcontent.cgi?article=2767&context=theses.

Rogers, J.A., Someya, T., Huang, Y., 2010. Materials and mechanics for stretchable electronics. Science 327, 1603–1607. http://dx.doi.org/10.1126/science.1182383.

Rumsey, M.A., Paquette, J.A., 2008. Structural health monitoring of wind turbine blades. In: Ecke, W., Peters, K.J., Meyendorf, N.G. (Eds.), Smart Sensor Phenomena, Technology, Networks, and Systems 2008, SPIE. http://dx.doi.org/10.1117/12.778324.

Saleem, H., Downey, A., Laflamme, S., Kollosche, M., Ubertini, F., 2015. Investigation of dynamic properties of a novel capacitive-based sensing skin for nondestructive testing. Mater. Eval. 73, 1384–1391. http://www.scopus.com/inward/record.url?eid=2-s2.0-84948392242&partnerID=MN8TOARS.

Schulz, M.J., Sundaresan, M.J., 2006. Smart Sensor System for Structural Condition Monitoring of Wind Turbines: May 30, 2002-April 30, 2006. National Renewable Energy Laboratory. https://pdfs.semanticscholar.org/a38f/83bec8c8d0d5084554f679d2726f07c30baf.pdf.

Sohn, H., Farrar, C.R., Hemez, F.M., Shunk, D.D., Stinemates, D.W., Nadler, B.R., Czarnecki, J.J., 2003. A Review of Structural Health Monitoring Literature: 1996–2001. Los Alamos National Laboratory, USA. https://www.researchgate.net/profile/Hoon_Sohn/publication/236499183_A_Review_of_Structural_Health_Review_of_Structural_Health_Monitoring_Literature_1996-2001/links/552518450cf2b123c517828c.pdf.

VanderMeer, J.B., Mueller-Stoffels, M., 2014. Wind-geothermal-diesel Hybrid Micro-grid Development: a Technical Assessment for Nome (AK. Ph.D. thesis. M. Sc. Thesis). University of Oldenburg. http://acep.uaf.edu/media/88917/NomeAssesmentPaperforBerkley_Revised.pdf.

Wang, L., Quant, R., Kolios, A., 2016. Fluid structure interaction modelling of horizontal-axis wind turbine blades based on CFD and FEA. J. Wind Eng. Ind. Aerodynam. 158, 11–25. http://dx.doi.org/10.1016/j.jweia.2016.09.006.

Xu, Y., Jiang, F., Newbern, S., Huang, A., Ho, C.M., Tai, Y.C., 2003. Flexible shear-stress sensor skin and its application to unmanned aerial vehicles. Sens. Actuators A Phys. 105, 321–329. http://dx.doi.org/10.1016/s0924-4247(03)00230-9.

Yao, Y., Glisic, B., 2015. Detection of steel fatigue cracks with strain sensing sheets based on large area electronics. Sensors 15, 8088–8108. http://dx.doi.org/10.3390/s150408088.

Zou, Y., Tong, L., Steven, G.P., 2000. Vibration-based model-dependent damage (delamination) identification and health monitoring for composite structures a review. J. Sound Vib. 230, 357–378. http://dx.doi.org/10.1006/jsvi.1999.2624.